

# Observation of H<sub>2</sub> Evolution and Electrolyte Diffusion on MoS<sub>2</sub> Monolayer by In Situ Liquid-Phase Transmission Electron Microscopy

Jihoon Kim, Anseong Park, Joodeok Kim, Seung Jae Kwak, Jae Yoon Lee, Donghoon Lee, Sebin Kim, Back Kyu Choi, Sungin Kim, Jimin Kwag, Younhwa Kim, Sungho Jeon, Won Chul Lee, Taeghwan Hyeon, Chul-Ho Lee, Won Bo Lee,\* and Jungwon Park\*

Unit-cell-thick MoS<sub>2</sub> is a promising electrocatalyst for the hydrogen evolution reaction (HER) owing to its tunable catalytic activity, which is determined based on the energetics and molecular interactions of different types of HER active sites. Kinetic responses of MoS<sub>2</sub> active sites, including the reaction onset, diffusion of the electrolyte and H<sub>2</sub> bubbles, and continuation of these processes, are important factors affecting the catalytic activity of MoS<sub>2</sub>. Investigating these factors requires a direct real-time analysis of the HER occurring on spatially independent active sites. Herein, the H<sub>2</sub> evolution and electrolyte diffusion on the surface of MoS<sub>2</sub> are observed in real time by in situ electrochemical liquid-phase transmission electron microscopy (LPTM). Time-dependent LPTM observations reveal that different types of active sites are sequentially activated under the same conditions. Furthermore, the electrolyte flow to these sites is influenced by the reduction potential and site geometry, which affects the bubble detachment and overall HER activity of MoS<sub>2</sub>.

lowering the reaction barrier in the transition state.<sup>[1–4]</sup> It is well-known that the active sites located on the catalyst surface promote important HER steps, including reactant adsorption (Volmer step), electrochemical H<sub>2</sub> desorption (Heyrovsky step), and chemical H<sub>2</sub> desorption (Tafel step).<sup>[5]</sup> MoS<sub>2</sub> monolayer is a promising HER catalyst because its HER activity can be easily tuned by manipulating the type and density of catalytically active sites.<sup>[6,7]</sup> The basal plane of 2H-MoS<sub>2</sub> is chemically inert because of the fully occupied Mo d-orbitals. By contrast, the Mo-exposed centers located at point defects (S vacancies) and edge sites of MoS<sub>2</sub> layers contain dangling bonds with unoccupied 4d-orbitals.<sup>[8]</sup> These dangling bonds with unsaturated 4d-electrons locally increase

## 1. Introduction


The hydrogen evolution reaction (HER) via electrolytic water splitting facilitates sustainable H<sub>2</sub> production without the use of hydrocarbon sources. However, water electrolysis is considerably limited by its large activation energy barrier. Electrocatalysts can be employed for an energetically favorable HER by

the electrical conductivity by tuning the bandgap energy, while the local strain induced by the vacant atoms strongly affects the electronic structure. The upshifts of d-band centers at the edge and point defects suppress electron filling in the anti-bonding states, increasing the charge transfer density and H affinity.<sup>[9]</sup> Moreover, the Gibbs free energy for H adsorption is significantly reduced by the presence of Mo-exposed active

J. Kim, A. Park, J. Kim, S. J. Kwak, D. Lee, S. Kim, B. K. Choi, S. Kim, J. Kwag, Y. Kim, T. Hyeon, W. B. Lee, J. Park  
School of Chemical and Biological Engineering  
and Institute of Chemical Processes  
Seoul National University  
Seoul 08826, Republic of Korea  
E-mail: wblee@snu.ac.kr; jungwonpark@snu.ac.kr

J. Kim, J. Kim, B. K. Choi, S. Kim, J. Kwag, T. Hyeon, J. Park  
Center for Nanoparticle Research  
Institute for Basic Science (IBS)  
Seoul 08826, Republic of Korea

J. Y. Lee, C.-H. Lee  
KU-KIST Graduate School of Converging Science and Technology  
Korea University  
Seoul 02841, Republic of Korea

 The ORCID identification number(s) for the author(s) of this article can be found under <https://doi.org/10.1002/adma.202206066>.

S. Jeon, W. C. Lee  
Department of Mechanical Engineering  
BK21 FOUR ERICA-ACE Center  
Hanyang University  
Ansan 15588, Republic of Korea

C.-H. Lee  
Department of Integrative Energy Engineering  
Korea University  
Seoul 02841, Republic of Korea

J. Park  
Institute of Engineering Research  
College of Engineering  
Seoul National University  
Seoul 08826, Republic of Korea

J. Park  
Advanced Institutes of Convergence Technology  
Seoul National University  
Seoul 08826, Republic of Korea

DOI: 10.1002/adma.202206066

sites. Such a fundamental understanding of the origin of HER activity enables the structural engineering of MoS<sub>2</sub> aimed at increasing its catalytic activity.<sup>[10–12]</sup> However, it is not clear how different types of active sites kinetically respond to an electric potential, where the MoS<sub>2</sub> surface is electrochemically activated during its interaction with the electrolyte. Therefore, it is necessary to elucidate the effects produced by different types of active sites on activation kinetics, their reaction progressions, and rate-limiting factors affecting HER activities.

The H<sub>2</sub> gas evolution occurring at local active sites during HER presumably induces kinetic perturbation due to the formation of gas–liquid–solid interfaces.<sup>[13,14]</sup> For instance, the interfaces produced by H<sub>2</sub> bubbles on the MoS<sub>2</sub> surface create convection in the adjacent liquid electrolyte, which can accelerate the mass transfer of electrolyte molecules to the active sites.<sup>[15]</sup> However, if H<sub>2</sub> bubbles remain on the MoS<sub>2</sub> surface for an extended time, they are likely to reduce the electrolyte flow to the active sites. The impeded electrolyte diffusion by the adsorbed bubbles critically decreases the total current density and HER catalytic efficiency, as previously reported in studies of the bubble-pinning effect on the MoS<sub>2</sub> layer.<sup>[16,17]</sup> Thus, reducing the contact time of H<sub>2</sub> bubbles with the MoS<sub>2</sub> surface is an important factor affecting the HER duration by opening an electrolyte diffusion pathway. The adsorption of bubbles can be manipulated by controlling the wetting of the liquid electrolyte with the catalyst surface.<sup>[18]</sup> However, the surface wetting of H<sub>2</sub> bubbles and electrolyte molecules on MoS<sub>2</sub> and its effect on the HER progress remain unexplored because the direct observation of the HER occurring on the MoS<sub>2</sub> surface at a nanoscale spatial resolution is a challenging task. In this regard, in situ liquid-phase transmission electron microscopy (LPTEM) can directly visualize the H<sub>2</sub> evolution process at the individual active sites of the MoS<sub>2</sub> monolayer under electrical biasing, which facilitates the time-dependent analysis of the bubble formation and fluid dynamic behavior of the electrolyte.<sup>[19–25]</sup> Herein, in situ electrochemical LPTEM is used for the real-time observation of the HER on the MoS<sub>2</sub> surface. The obtained results reveal that different types of catalytic active sites, such as strained defects, point defects, and edge sites, are sequentially activated under the same conditions. In addition, the direct nanometer-scale monitoring of the H<sub>2</sub> bubble formation confirms the active site-specific wettability of the electrolyte on the MoS<sub>2</sub> surface and kinetic detachment of surface H<sub>2</sub> bubbles caused by the competition between the bubble and electrolyte wetting processes on MoS<sub>2</sub> during HER.

## 2. Results and Discussion

### 2.1. In Situ Electrochemical LPTEM Analysis of HER on MoS<sub>2</sub> Monolayer

The LPTEM-based experimental setup for the in situ observation of the MoS<sub>2</sub>-activated HER is schematically illustrated in **Figure 1a**. The top chip of the liquid cell contains three electrodes micropatterned on the electron transparent SiN<sub>x</sub> window. The MoS<sub>2</sub> monolayers grown by chemical vapor deposition (CVD) are transfer-printed onto a glassy carbon (GC)

working electrode (WE) by a surface energy-assisted transfer method.<sup>[26]</sup> C<sub>s</sub>-corrected scanning transmission electron microscopy (C<sub>s</sub>-STEM) observations of the transferred MoS<sub>2</sub> show the presence of covalently bonded Mo and S atoms in the MoS<sub>2</sub> monolayers, confirming their successful transfer printing (**Figure S1**, Supporting Information). Raman spectrum and mapping data also verify the complete transfer of MoS<sub>2</sub> onto the microchip (**Figure S2**, Supporting Information). The strong intensities of the Raman (E<sub>2g</sub><sup>1</sup> and A<sub>1g</sub> vibrational modes) peaks indicate high crystallinity of the MoS<sub>2</sub> monolayers.<sup>[27]</sup> The top chip with the transferred MoS<sub>2</sub> is assembled with the bottom chip to maintain perfect sealing of the liquid cell under the ultrahigh vacuum of the transmission electron microscopy (TEM) column. The liquid cell is also filled with an electrolyte (0.1 N H<sub>2</sub>SO<sub>4</sub> aqueous solution) by a liquid flow system. A negative potential for electrochemical reduction is applied to the WE during in situ LPTEM imaging, which is used to directly monitor the H<sub>2</sub> evolution process at the HER active sites of the MoS<sub>2</sub> layer. The time-resolved TEM images as increasing the negative reduction potential show the H<sub>2</sub> bubble formation and electrolyte flow on the MoS<sub>2</sub> layer (**Figure 1b** and **Movie S1** (Supporting Information)). Deep-learning-based denoiser is introduced to improve the spatial resolution of the in situ LPTEM images. The linear sweep voltammetry (LSV) curve corresponding to the TEM images is presented in **Figure 1c**. To confirm the reliable electrochemical behavior of the MoS<sub>2</sub> monolayers in the bulk, the HER of the MoS<sub>2</sub> layer in a beaker cell is performed using a large GC electrode containing MoS<sub>2</sub> flakes. The onset potential (−0.309 V<sub>RHE</sub>) and Tafel slope (107 mV dec<sup>−1</sup>) are obtained from the constructed LSV and Tafel plots (**Figure S3**, Supporting Information). These parameters are consistent with previously reported values, which demonstrate the robustness of MoS<sub>2</sub> monolayers.<sup>[28]</sup> We also confirm that the onset potential of the MoS<sub>2</sub>-activated HER in the liquid cell is −0.756 V<sub>RHE</sub>. In (i) and (ii), the reduction current increases within a small potential range, and H<sub>2</sub> bubbles are not clearly visible in the TEM images at a given magnification (**Figure 1b,c**), which is used for minimizing the electron beam damage (beam dose rate: <0.247 e<sup>−</sup> Å<sup>−2</sup> s<sup>−1</sup>). We confirm that the MoS<sub>2</sub> monolayers are stable at the electron beam dose of 0.247 e<sup>−</sup> Å<sup>−2</sup> s<sup>−1</sup> during in situ LPTEM imaging (**Figure S4**, Supporting Information). As the reduction potential is increased to more negative values, direct observation of the H<sub>2</sub> bubble formation becomes possible. Hydrogen bubbles are visualized by the bright image contrast in the sequential TEM images, while the local aggregation of electrolyte molecules induced by the outward electrolyte flow from the bubble growth location is shown by the dark contrast. The different contrasts of H<sub>2</sub> bubbles and electrolyte originate from the material density and thickness related to the electron beam deflection.<sup>[29]</sup> In the medium potential range ((ii) and (iii)), the regions with the bright and dark contrasts appear transiently, as confirmed by the corresponding intensity profiles (**Figure 1d**). It is confirmed that the dark contrast in the images is not emerged from the electron-beam-induced damage (**Figure S5**, Supporting Information). Frequent alternation of the bright and dark contrast regions indicates the dynamic H<sub>2</sub> evolution and its association with the electrolyte flow. The gas products generated inside the liquid cell

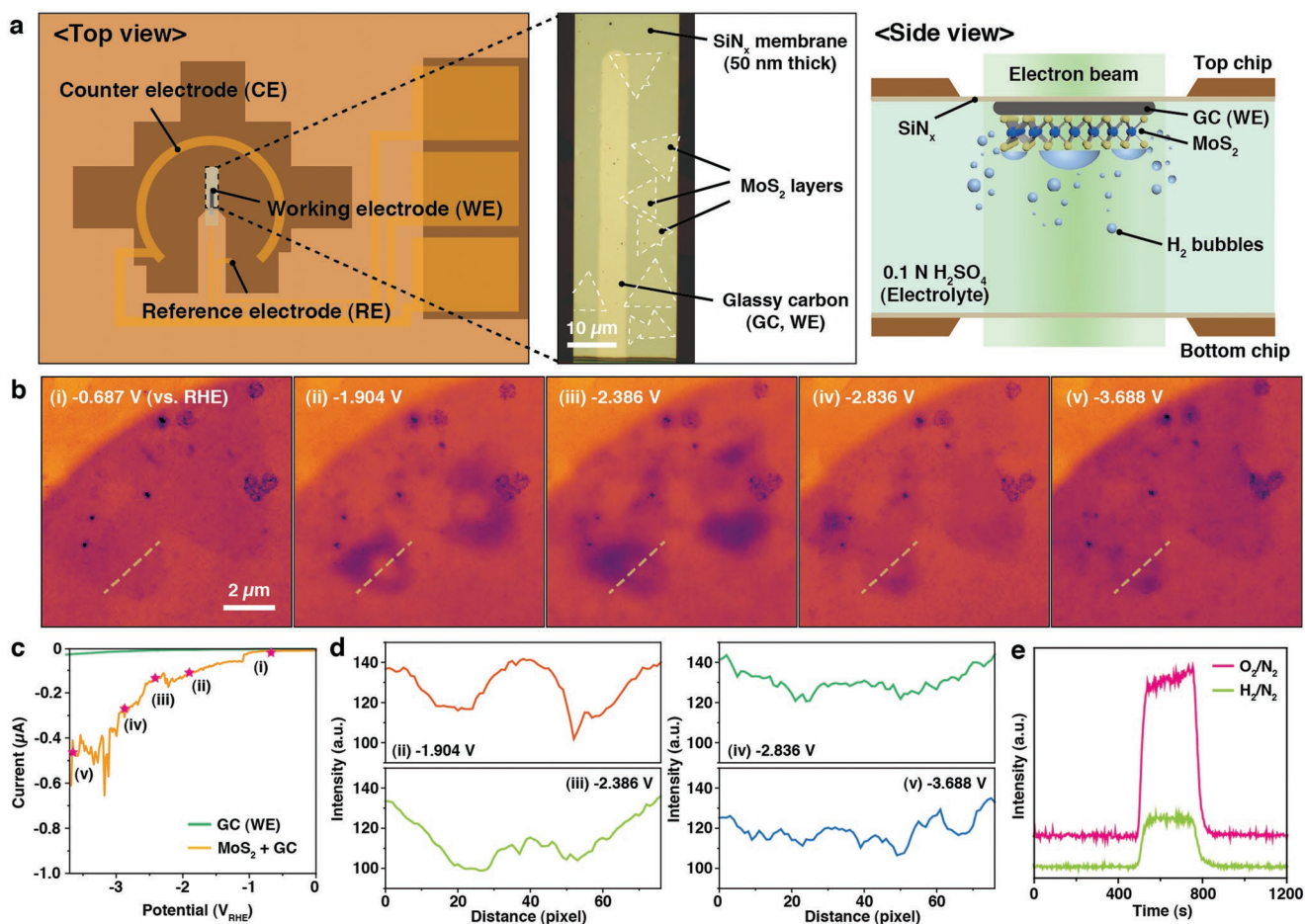


**Figure 1.** In situ electrochemical liquid-phase transmission electron microscopy (LPTM) for hydrogen evolution reaction (HER) of MoS<sub>2</sub> monolayer. a) Schematic illustration and optical microscopy image of LPTM setup filled with the acidic electrolyte (0.1 N H<sub>2</sub>SO<sub>4</sub>). The white dashed triangles indicate MoS<sub>2</sub> monolayers transferred on the microchip. Scale bar: 10 μm. b) Time-resolved LPTM images with increasing the applied reduction potential (0 to -3.7 V<sub>RHE</sub>). Scale bar: 2 μm. c) Linear sweep voltammogram (LSV) during in situ electrochemical LPTM imaging. Applied potentials corresponding to the TEM images are indicated by the magenta stars (i) to (v). d) Intensity profiles from the dashed lines in (b). e) Mass spectrometry of the gas products collected from the liquid cell after in situ LPTM experiment.

are collected and analyzed by mass spectrometry (Figure 1e). Among these products, hydrogen detection confirms the successful H<sub>2</sub> evolution during the in situ electrochemical LPTM analysis. In the high potential range ((iv) and (v)), the electrolyte wetting of the electrode surface is enhanced by the large applied potential,<sup>[30]</sup> which promotes the full coverage of the MoS<sub>2</sub> surface with electrolyte molecules. The continuous supply of the electrolyte induced by the high reduction potential intensifies the production of H<sub>2</sub> gas and its prompt desorption from the MoS<sub>2</sub> surface fully covered by electrolyte species (Figure S6, Supporting Information). The gentle slope of the intensity profile indicates enhanced electrolyte wetting of the MoS<sub>2</sub> surface. The higher reduction current measured by LSV supports this conclusion. The observed fluctuations of the LSV curve are possibly caused by the repeated supply and blockage of electrolyte molecules by the adsorbed bubbles at the active sites. As the bubbles are formed with short lifetimes in the confined space of the liquid cell, they can locally inhibit mass transfer and decrease the current density.

## 2.2. Sequential H<sub>2</sub> Evolution from Different Types of HER Active Sites

The 3D geometry of the transferred MoS<sub>2</sub> on the GC electrode is schematically illustrated in Figure 2a. Atomic resolution C<sub>s</sub>-STEM images display possible HER active sites of the CVD-grown MoS<sub>2</sub> layer including point defects (S vacancies) and Mo zigzag (Mo-zz) edges (Figure 2b). The height profile of the GC electrode measured by atomic force microscopy shows the curvature of the electrode edge that can induce a strain effect on the overlaid MoS<sub>2</sub> layer (Figure S7, Supporting Information). When a constant potential of -2.2 V<sub>RHE</sub> is applied to the WE, H<sub>2</sub> bubble formation is observed by the time-resolved LPTM at three different types of active sites, including strained defects, point defects, and MoS<sub>2</sub> edges (Figure 2c and Movie S2 (Supporting Information)). A chronoamperometry curve obtained at an applied potential of -2.2 V<sub>RHE</sub> is presented in Figure S8a (Supporting Information). The first activation at the early stage of the HER occurs at strained MoS<sub>2</sub> defects. Dynamic H<sub>2</sub>

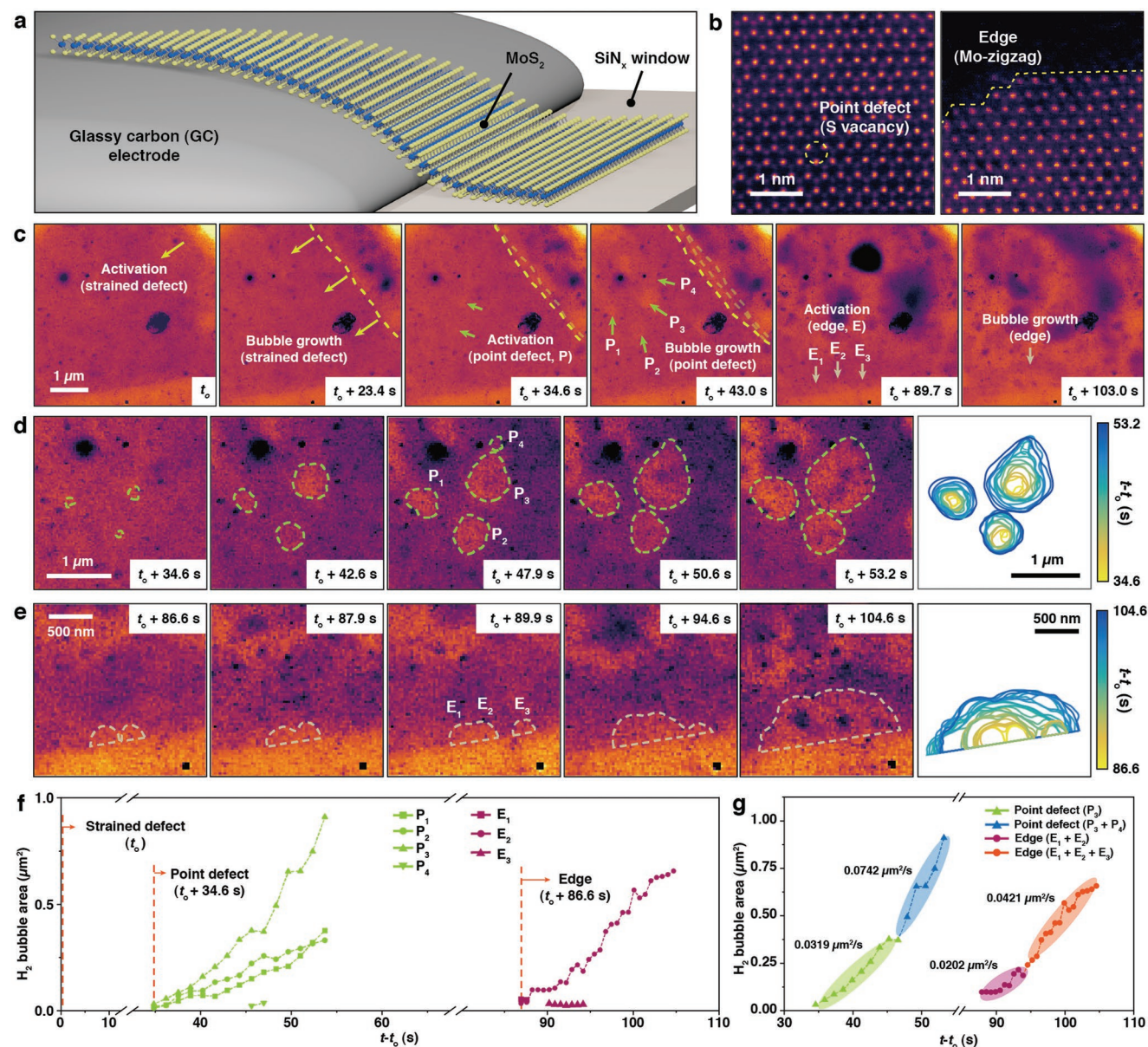


**Figure 2.** Catalytic active sites of MoS<sub>2</sub> monolayer and their sequential activation. a) Schematics of the geometry of the working electrode (GC) and MoS<sub>2</sub> electrocatalyst. b) Denoised C<sub>5</sub>-STEM images of the point defect (S vacancy) and edge (Mo-zigzag) sites of the MoS<sub>2</sub> monolayer. Scale bars: 1 nm. c) Real-time LPTM images during HER process at various types of active sites of the MoS<sub>2</sub> layer. Scale bar: 1 μm. H<sub>2</sub> evolution at the each of the active sites are designated by the colored arrows. d,e) LPTM images for H<sub>2</sub> bubble growth at the point defects (P<sub>1</sub>–P<sub>4</sub>) and edge sites (E<sub>1</sub>–E<sub>3</sub>), respectively. Contours of the gas–liquid–solid interfaces are indicated by dashed lines. Time-dependent contour lines are displayed in the progress of time at the right side of the images. Scale bars: 1 μm in (d) and 500 nm in (e), respectively. f) H<sub>2</sub> bubble area versus time plot for analyzing the bubble growth rate for the active sites (P<sub>1</sub>–P<sub>4</sub> and E<sub>1</sub>–E<sub>3</sub>). g) H<sub>2</sub> bubble area versus time plot of the merged bubbles (P<sub>3</sub> + P<sub>4</sub> and E<sub>1</sub> + E<sub>2</sub> + E<sub>3</sub>) for the point defects and edge sites, respectively.

bubble formation from the strained defects is visualized by the alternation of the bright and dark contrasts in the time-series LPTM images (Figure S9, Supporting Information). H<sub>2</sub> bubbles rapidly evolve from several strained defect sites, resulting in a line propagation, as indicated by the yellow dashed lines in Figure 2c. Subsequently, point defects (P<sub>1</sub>–P<sub>4</sub>) of the MoS<sub>2</sub> layer initiate the formation of H<sub>2</sub> bubbles at  $t_0 + 34.6$  s during LPTM imaging. Neighboring point defects independently

generate H<sub>2</sub> bubbles that grow steadily at each site, as shown in the magnified time-series LPTM images (Figure 2d). The bubbles that evolve from the P<sub>3</sub> and P<sub>4</sub> sites collapse and merge after the time of  $t_0 + 47.9$  s. Subsequently, the edge sites (E<sub>1</sub>–E<sub>3</sub>) of the MoS<sub>2</sub> monolayer are activated (Figure 2e). The bubbles evolved from the E<sub>1</sub> and E<sub>2</sub> sites merge during the early stage of bubble formation. The merged bubble (E<sub>1</sub> + E<sub>2</sub>) grows faster than the bubble evolved from a single site (E<sub>3</sub>) due to the

high density of the Mo-*zz* centers. To determine the growth rate of evolving H<sub>2</sub> bubbles, their contour areas are tracked using homebuilt MATLAB codes and plotted with respect to time (Figure 2f). The starting points of HER activation obtained for different types of active sites are indicated by the orange dashed lines. Sequential activation in the order of strained defect, point defect, and edge sites is confirmed, a consistent trend for the HER activity reported in the previous study.<sup>[7]</sup> Because the applied electric potential is much larger than the onset potential (−0.756 V<sub>RHE</sub> in Figure 1c), the observed sequential H<sub>2</sub> evolution indicates kinetically different responses of the active sites. Monitoring the bubble formation process on the nanometer scale shows the heterogeneity of the bubble growth rates obtained for different active sites of the same type (P<sub>1</sub>–P<sub>4</sub>) because the degree of S vacancy clustering can vary from site to site (Figure S10, Supporting Information).<sup>[31–33]</sup> The H<sub>2</sub> bubbles evolved from the edge sites of the MoS<sub>2</sub> monolayer (E<sub>1</sub>–E<sub>3</sub>) also grow at different rates due to the different Mo-*zz* densities (Figure 2e,f). The largest growth rates determined for each group of point defects and edge sites are quite different (0.0319 μm<sup>2</sup> s<sup>−1</sup> for P<sub>3</sub> and 0.0202 μm<sup>2</sup> s<sup>−1</sup> for merged E<sub>1</sub> and E<sub>2</sub>; see Figure 2g). The merging of bubbles increases the growth rate owing to the larger number of active sites. The growth rate of the merged bubble evolved from the P<sub>3</sub> and P<sub>4</sub> sites is equal to 0.0742 μm<sup>2</sup> s<sup>−1</sup>, which is 2.33 times larger than the bubble formation rate measured for a single P<sub>3</sub> defect site (0.0319 μm<sup>2</sup> s<sup>−1</sup>). The merged bubble evolved from the edge sites (E<sub>1</sub> + E<sub>2</sub> + E<sub>3</sub>) grows at a rate 0.0421 μm<sup>2</sup> s<sup>−1</sup>, 2.08 times faster than the bubble before merging (0.0202 μm<sup>2</sup> s<sup>−1</sup>). However, this merged bubble growth rate is 1.76 times lower than the growth rate of the merged bubble evolved from point defects (0.0742 μm<sup>2</sup> s<sup>−1</sup>).

### 2.3. Potential-Induced Electrolyte Insertion to the Active Sites

The LPTM observations of the MoS<sub>2</sub>-activated HER describe the H<sub>2</sub> bubble growth and interaction processes as well as the related electrolyte transport, as shown in the TEM images acquired at an applied potential of −2.2 V<sub>RHE</sub> (Figure 3a). The merged bubble undergoes a typical interface relaxation process, changing its original shape with a negative curvature into a spherical morphology, as indicated by the contour map and circularity changes of the merged bubble depicted in Figure 3b,d, respectively. The circularity of the bubble rapidly decreases after the merging events (I and II), as denoted by the dashed lines in Figure 3d. The bubble interface immediately relaxes to minimize the surface free energy, as confirmed by the circularity recovery. The growing H<sub>2</sub> bubbles are pinned onto the MoS<sub>2</sub> layer, which confirms the strong adhesion between MoS<sub>2</sub> surface and H<sub>2</sub> bubbles observed in a previous study.<sup>[34]</sup> The pinned bubbles on the catalyst surface have been considered a source of deterioration of the HER catalytic activity, which can block the electrolyte supply pathway to the active sites. However, the defect sites of the MoS<sub>2</sub> layer blocked by the bubbles can maintain their activity due to the continuous supply of the electrolyte. The enhanced electrolyte surface wetting by the applied potential enables electrolyte penetration through the gas–solid interface (Figure 3c). The electrolyte diffused under-

neath the merged bubble can be transferred across the necking point (*t*<sub>0</sub> + 63.1 s in Figure 3c), which promotes the activation of defect sites, as confirmed by the continuous growth of H<sub>2</sub> bubbles at the blocked active sites. To enhance the potential-induced diffusion of electrolyte molecules through the gas–solid interface, a relatively large potential of −4.2 V<sub>RHE</sub> has been applied in this work (Figure 3e and Figure S8b and Movie S3 (Supporting Information)). A blinking of the dark contrast is observed at the point defects, indicating the rapid and frequent insertion of electrolyte molecules, while the size of the detached bubbles is smaller than that of the bubbles generated at the medium applied potential of −2.2 V<sub>RHE</sub>. This phenomenon indicates that the enhanced electrolyte wetting of the MoS<sub>2</sub> surface at a high potential accelerates the electrolyte flow to the active sites and causes frequent detachment of the as-formed H<sub>2</sub> bubbles. However, at the edge sites, blinking of the dark contrast is hardly observed, while H<sub>2</sub> bubbles gradually grow along the periphery of the MoS<sub>2</sub> layer. We have also measured the average image intensity of five lateral pixels along the vertical line passing through the point defects, edges, and GC background and tracked the averaged intensity profile during the HER at a high applied potential of −4.2 V<sub>RHE</sub> (Figure 3f). The average intensities are normalized by the background intensity (*I*<sub>BG</sub>) of the GC electrode located at a large distance from the MoS<sub>2</sub> layer (Figure 3g). The defect sites of the MoS<sub>2</sub> layer exhibit a rapid change in the bright and dark contrasts, while the MoS<sub>2</sub> edges maintain the bright contrast. The average intensities of the defect sites (*I*<sub>Defect</sub>/*I*<sub>BG</sub>) largely fluctuate in the range lower than that obtained for the GC electrode (*I*<sub>GC</sub>/*I*<sub>BG</sub>), which suggests that fast H<sub>2</sub> bubbling and electrolyte insertion repeatedly occur at the defect sites. However, the average intensities of the edge sites (*I*<sub>Edge</sub>/*I*<sub>BG</sub>) fluctuate marginally and exhibit higher values than *I*<sub>GC</sub>/*I*<sub>BG</sub>, which implies that the electrolyte supply from the outside of the MoS<sub>2</sub> edge is restricted. Such a potential-induced electrolyte insertion process occurs differently at the point defect and edge sites, as schematically illustrated in Figure 3h. Thus, it is supposedly possible that the potential-induced electrolyte insertion affects H<sub>2</sub> evolution rates of the active sites listed in Figure 2g. The H<sub>2</sub> bubbles evolved from the activated defect sites of the MoS<sub>2</sub> layer grow isotropically, which allows uniform penetration of the liquid electrolyte along the entire periphery of the formed bubble. By contrast, the H<sub>2</sub> bubbles growing on the MoS<sub>2</sub> edge sites spill over toward the basal plane of the MoS<sub>2</sub> layer due to the strong adhesion between these bubbles and the MoS<sub>2</sub> surface. The geometry of the MoS<sub>2</sub> edge promotes the anisotropic potential-induced insertion of electrolyte molecules. As the growing bubble covers the basal plane and the edge site, it is possible to further limit the electrolyte supply. It is different from the situation of point defect sited on the basal plane, where the electrolyte supply is radially uniform (Figure 3h). In addition, displacement heatmaps obtained from molecular dynamics (MD) simulation present that the mobility of the electrolyte at the edge of the MoS<sub>2</sub> layer (Figure S11, Supporting Information) is inherently low even in the absence of bubbles. Therefore, the geometry and directionality of H<sub>2</sub> bubbling are related to the electrolyte flow to the active sites, one of the important factors associated with the kinetic duration of the local HER activity of the MoS<sub>2</sub> layer.

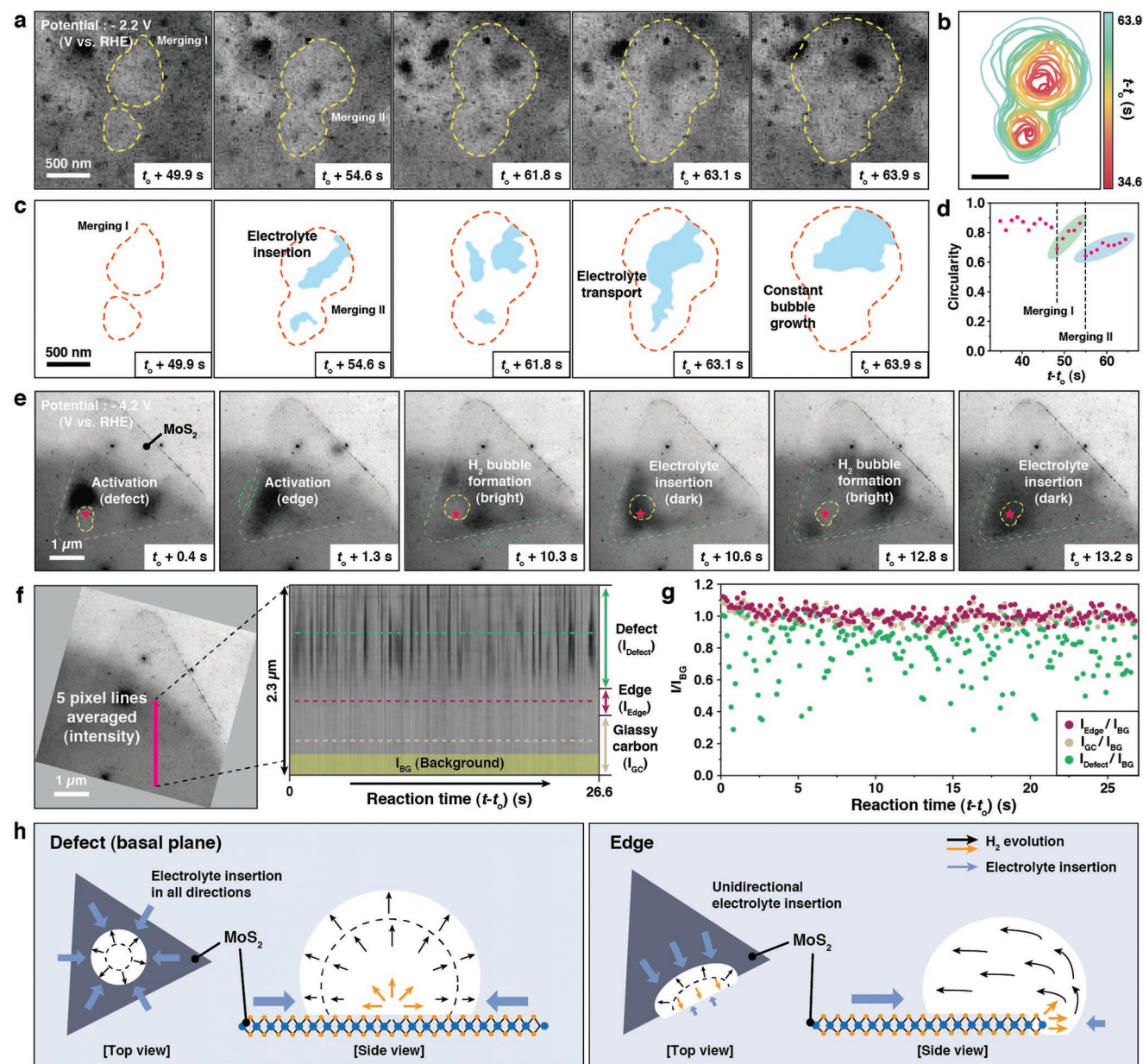


**Figure 3.** Surface relaxation of H<sub>2</sub> bubble and potential-induced electrolyte insertion process during HER. a) In situ LPTM images of H<sub>2</sub> evolution and bubble merging process under the applied potential of  $-2.2 V_{\text{RHE}}$ . Scale bar, 500 nm. b) Contour lines of the gas–liquid interfaces with the increased time. Scale bar: 500 nm. c) Contour maps of the gas–liquid–solid interfaces and the inserted electrolyte. The orange dashed lines and sky blue areas show the gas–liquid–solid interfaces and electrolyte inserted into the bubble, respectively. Scale bar: 500 nm. d) Circularity versus time plot extracted from the gas–liquid–solid interface contours. e) LPTM images of the H<sub>2</sub> bubble formation and electrolyte insertion of the MoS<sub>2</sub> layer under the reduction potential of  $-4.2 V_{\text{RHE}}$ . Bubbles are indicated by yellow (defect) and green (edge) dashed lines in TEM images. Scale bar: 1  $\mu\text{m}$ . f) LPTM image and averaged intensity plot from 5 lateral pixel lines in the progress of time. g) Normalized intensity ( $I/I_{\text{BG}}$ ) plot for the point defect, edge, and glassy carbon indicated by green, purple, and gray dots, respectively.  $I_{\text{BG}}$  is the averaged intensity value obtained from the light-green area in the averaged intensity plot of (f). h) Schematic illustration of the H<sub>2</sub> bubble evolution and growth at the point defect (left) and edge (right) of the MoS<sub>2</sub> layer.

## 2.4. Surface Wetting of the Electrolyte and H<sub>2</sub> Bubbles on the MoS<sub>2</sub> Monolayer

MD simulation results reveal that the local environment near the MoS<sub>2</sub> surface can be controlled by varying the external electric field strength applied to the system (Figure 4a). The negatively charged MoS<sub>2</sub> surface is described by the surface the

electric field enters. The number densities of the hydronium (H<sub>3</sub>O<sup>+</sup>) and hydrogen sulfate (HSO<sub>4</sub><sup>-</sup>) ions exhibit electric field strength dependencies on their affinities toward the MoS<sub>2</sub> layer at all concentrations (Figure 4b and Figure S12 (Supporting Information)). Upon increasing the electric field strength from 0 to 4 V nm<sup>-1</sup>, more H<sub>3</sub>O<sup>+</sup> ions which generates H<sub>2</sub> bubbles accumulate on the MoS<sub>2</sub> surface, while the number of HSO<sub>4</sub><sup>-</sup>

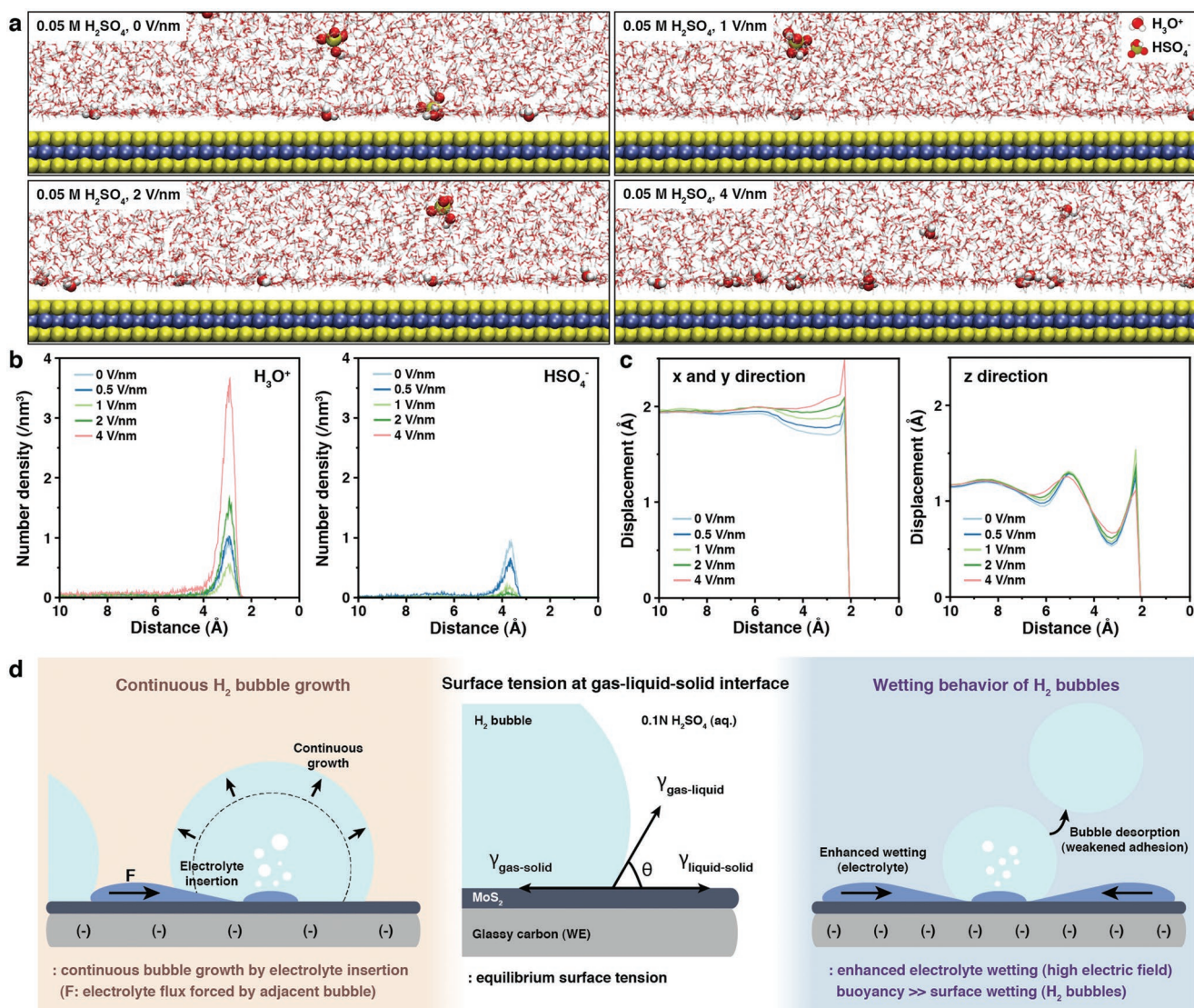


**Figure 4.** MD simulation and surface wetting of the electrolyte and H<sub>2</sub> bubble during MoS<sub>2</sub> HER. a) Schematic illustration of the distributions of the H<sub>3</sub>O<sup>+</sup> and HSO<sub>4</sub><sup>-</sup> ions and water molecules with the presence of static external electric fields (0, 1, 2, and 4 V nm<sup>-1</sup>). b) Number density plots (in the z-direction) of hydronium (H<sub>3</sub>O<sup>+</sup>, left) and hydrogen sulfate ions (HSO<sub>4</sub><sup>-</sup>, right) of 0.05 m system with the presence of static external electric fields (0, 0.5, 1, 2, and 4 V nm<sup>-1</sup>). c) Lateral (x- and y-directions, left) and vertical (z-direction, right) displacement plots of the water molecules of 0.05 m system with the presence of static external electric fields (0, 0.5, 1, 2, and 4 V nm<sup>-1</sup>). d) Schematic illustration of the potential-induced electrolyte wetting in the H<sub>2</sub> bubble formation and desorption processes.

ions near the MoS<sub>2</sub> surface decreases. The lateral (in the x- and y-directions) and vertical (in the z-direction) displacements of the water molecules increase as the applied external electric fields strengthen (Figure 4c), indicating that the stronger electric fields lead to the increase in mobility of electrolyte molecules near the MoS<sub>2</sub> surface.

These results suggest that surface wetting and the desorption of H<sub>2</sub> bubbles are key factors for the HER continuation that are strongly influenced by the interactions between the electrolyte and MoS<sub>2</sub> layer and can be modulated by the applied electric potential. Different scenarios of this behavior are illustrated in Figure 4d. For a static bubble on the MoS<sub>2</sub> surface, the surface tensions  $\gamma_{\text{gas-solid}}$ ,  $\gamma_{\text{gas-liquid}}$ , and  $\gamma_{\text{liquid-solid}}$  are equilibrated at the triple point of the gas-liquid-solid interface, as shown in

the central scheme of Figure 4d. If the negatively charged MoS<sub>2</sub> surface attracts the electrolyte, including mobile H<sub>3</sub>O<sup>+</sup> ions (as observed in the case of a low reduction potential), it lowers the surface tension  $\gamma_{\text{liquid-solid}}$  and promotes competitive wetting of the bubbles and electrolyte molecules on the MoS<sub>2</sub> surface (the left scheme in Figure 4d). Under these conditions, the convective flux (F) of the electrolyte produced by the adjacent growing bubbles can assist electrolyte insertion into the active sites. These effects facilitate the bubble formation by the continuous electrolyte flow to the active sites. The potential-induced insertion of the electrolyte can be accelerated by applying a large reduction potential, as illustrated by the right scheme of Figure 4d. In this case, the electrolyte with enhanced surface wetting occupies the bubble contact area, while the weakened

adhesive force of  $H_2$  bubbles expedites the detachment of the as-grown bubbles from the  $MoS_2$  surface. As a result, applying a large reduction potential leads to the fast detachment of small bubbles and dynamic insertion of the electrolyte into the active sites, which is consistent with the experimental results presented in Figure 3c.

### 3. Conclusion

The obtained in situ electrochemical LPTEM data reveal that different types of active sites, including strained defects, point defects, and edge sites of the  $MoS_2$  layer, are sequentially activated under electrical biasing conditions. The electrolyte surface wetting can be enhanced by applying a reduction potential, which facilitates the electrolyte flow to the active sites. The potential-induced electrolyte insertion strongly depends on the active site geometry and bubbling directionality, resulting in different growth rates of  $H_2$  bubbles for point defects and edges of the  $MoS_2$  layer. These results indicate that the surface wetting of electrolyte on the  $MoS_2$  layer is an important factor affecting the continuous  $H_2$  evolution and HER activity. There is no doubt that there are other factors to consider in order to understand the activity and kinetics of HER on diverse types of active sites on the  $MoS_2$ . Atomic structural identity of defects, their density on  $MoS_2$  layer, and their structural stability in HER, when they are correlated with in situ observation for  $H_2$  bubble production dynamics, are likely the important information to have more quantitative understanding on the kinetics of  $MoS_2$  HER. In the current study, the spatial resolution is not enough to resolve structural identity of the active sites and their changes occurring during HER because of the limited resolution due to the presence of the electrolyte in LPTEM. Nonetheless, our study suggests that enhancing surface wetting and bubble detachment by selecting an appropriate electrolyte design is a useful strategy for the development of efficient electrocatalyst systems with high HER activities.

### 4. Experimental Section

**Characterization of  $MoS_2$  Monolayers:** Raman spectrum and spectral mapping were performed by using aberration-corrected spectrometer with laser wavelength of 532 nm (HEDA, NOST) to determine the thickness and crystallinity of  $MoS_2$  crystal.  $C_s$ -corrected STEM images operated at an acceleration voltage of 80 or 200 kV were obtained by using JEM ARM-200F (JEOL Ltd.) with a spherical aberration corrector (probe correction) installed in the National Center for Inter-University Research Facility at the Seoul National University (SNU). Atomic force microscopy was performed by using NX-10 (Park Systems) equipped with a single module flexure XY-scanner, installed in the Research Institute of Advanced Materials at the SNU.

**Transfer Printing of  $MoS_2$  Monolayers on the Microchip:** Polystyrene (PS) solution (9 g of polystyrene beads in 100 mL toluene) was deposited on  $MoS_2$  monolayer flakes on sapphire substrate by using a spin-coater (rotation speed: 1500 rpm, rotation time: 60 s). The substrate deposited by PS was baked out for strong adhesion between PS and  $MoS_2$  layers (at 90 °C for 5 min). After immersion of the substrate in deionized (DI) water, the PS and  $MoS_2$  film was manually peeled off from the sapphire substrate. The stripped film was transferred on the working electrode of the microchip (top chip) and immersed in toluene for 1 h to dissolve the PS film. After the PS dissolution, the microchip with the

as-transferred  $MoS_2$  layers was rinsed by acetone and blown by high-purity nitrogen gas.

**In Situ Liquid-Phase TEM Setup:** The liquid cell for LPTEM analysis was composed of top chip (6 mm × 4.5 mm × 300 μm) and bottom chip (2 mm × 2 mm × 300 μm). The top and bottom microchips included 50 nm thick electron transparent  $SiN_x$  window (window dimensions: 550 μm × 40 μm for the top and 550 μm × 50 μm for the bottom). Working electrode (WE), counter electrode (CE), and reference electrode (RE) were micropatterned on the top chip. Metal circuits were sealed with a spacer (SU-8, thickness: 500 nm). All microchips were purchased from Protochips. 0.1 N  $H_2SO_4$  aqueous solution was saturated with Ar gas for the prolonged bubbling time and used as the electrolyte in the liquid cell. Electrolyte was injected into the liquid cell by a liquid flow system (injection speed: 120 μL h<sup>-1</sup>). Potentiostat (Reference 600+, Gamry) was connected to the LPTEM holder (Poseidon, Protochips) for electrochemical experiments. In situ LPTEM experiments were performed by using JEM-2100F (JEOL Ltd.) operated at the acceleration voltage of 200 kV, equipped with an UltraScan 1000XP charge coupled device detector (Gatan). The electron dose rate during in situ LPTEM analysis was maintained to <0.247 e<sup>-</sup> Å<sup>-2</sup> s<sup>-1</sup> for minimizing the beam-induced damage. In situ LPTEM videos were recorded with a frame rate of 10 frames s<sup>-1</sup>.

**Electrochemical Measurement:** The electrochemical measurements for  $MoS_2$  HER were conducted with a three-electrode system in the liquid cell (WE: glassy carbon, CE and RE: platinum). The Pt reference electrode was calibrated in 0.1 N  $H_2SO_4$  solution. The GC WE was replaced with Pt WE for this calibration process. Cyclic voltammetry (CV) obtained using Pt WE and RE featured a typical CV profile of the platinum (Figure S13, Supporting Information), where the curve exhibited the Pt oxide reduction peak at 0 V (vs Pt) in 0.1 N  $H_2SO_4$  solution. The Pt–O reduction potential from Pt RE ( $V_{Pt}$ ) showed the shifted value of 0.8 V compared to the potential from reversible hydrogen electrode ( $V_{RHE}$ ) as the RE.<sup>[35]</sup> Therefore, the obtained  $V_{Pt}$  values were converted to the values of  $V_{RHE} - 0.8$  V ( $V_{RHE} = V_{Pt} + 0.8$  V). Bulk electrochemical experiments were performed using potentiostat (PGSTAT302N/FRA2, Autolab) and beaker cell (WE: glassy carbon plate, CE: Pt wire, RE: Ag/AgCl). Surface area of the GC WE used in the beaker cell was 5 cm<sup>2</sup>.

**Training and Denoising of In Situ LPTEM Images:** In the experiment, in situ TEM images were postprocessed to remove noise to improve visualization. Deep-learning-based denoiser was used based on unsupervised blind-spot denoising method<sup>[36]</sup> with customized neural network. To train model and inference denoised images, PyTorch- and Pytorch-lightning-<sup>[37,38]</sup> based homemade codes were used. Training datasets were generated by subsampling 256 × 256 sized image patches from TEM images. As data augmentation, patches were randomly rotated by 90°, 180°, 270°, and mirrored. Models were trained for every dataset with double NVIDIA RTX 2080Ti GPU, training and inference took about 4 h per dataset.

**MD Simulation:** The aqueous sulfuric acid solutions were comprised of hydronium ions, hydrogen sulfate ions, and water. Exact number of molecules, the corresponding salt concentrations,  $MoS_2$  slabs' end-to-end distance (z-axis), and box size were shown in Table S1 (Supporting Information) and system images were shown in Figure S14 (Supporting Information). Vacuum was added to top and bottom of the  $MoS_2$ /solvent system which was equal to the size of z length shown in Table S1 (Supporting Information). Defect  $MoS_2$  slab had 19 S-defect sites, where 18 S-defect sites were aligned with 3 × 6 matrix at the center and the other one at the left end of  $MoS_2$  slab (Figure S14c, left, Supporting Information). Defect  $MoS_2$  slab was placed at the bottom of defect  $MoS_2$  and strained  $MoS_2$  systems. Curvature radius of 10 nm was used to build strained  $MoS_2$  systems. The actual molar concentrations shown in Table S1 (Supporting Information) were in the order of 0.05, 0.248, and 0.487 M, but for convenience, concentrations would be marked as 0.05, 0.25, and 0.5 M. Density of each concentration was calculated from 10 ns NPT bulk simulation with a system size of 5551 water molecules and 5/25/50 pairs of  $H_3O^+$  and  $HSO_4^-$ . 20 ns NPT simulations were carried out on  $MoS_2$ /solvent systems in the presence of static external electric fields with intensities of 0.5, 1, 2, and 4 V nm<sup>-1</sup>,



respectively. For comparison, a simulation without an electric field was performed under same conditions. Number density profiles in the z-direction for ions were produced with last 5 ns of the NPT simulations. Water displacement analysis was conducted by averaging the movement of water molecules for 6 ps during the last 10 ns of the NVT simulations. All atom simulation was performed using GROMACS<sup>[39,40]</sup> molecular dynamics simulation package with optimized potentials for liquid simulation—all-atom (OPLS-AA) force field where the parameters were generated by LigParGen<sup>[41–43]</sup> force-field generator. Structure of MoS<sub>2</sub> slab was constructed using Inorganic Crystal Structure Database ID: 24000 and the force field parameters were taken from previous studies.<sup>[44,45]</sup> Charges of vacancy neighboring Mo were taken from density-derived electrostatic and chemical (DDEC) charge<sup>[46]</sup> and other charges of Mo at defect MoS<sub>2</sub> slab were set to 0.5108 to make the slab charge neutral. The cutoff distance for short-range van der Waals and Coulombic interactions was set to 1 nm. Long-range electrostatic interactions further than cutoff distance were calculated by particle mesh Ewald<sup>[47]</sup> method. Bond lengths were constrained by LINCS algorithm.<sup>[48]</sup> The integration timestep was set to 2 fs and temperature of the system was set to 298 K. Nosé–Hoover<sup>[49,50]</sup> thermostat and Parrinello–Rahman<sup>[51]</sup> pressure coupling were used in the simulation.

## Supporting Information

Supporting Information is available from the Wiley Online Library or from the author.

## Acknowledgements

J.K. and A.P. contributed equally to this work. J.K., J.K., B.K.C., S.K., J.K., T.H., and J.P. acknowledge the Institutes for Basic Science (Grant No. IBS-R006-D1). J.P. acknowledges the National Research Foundation of Korea (NRF) grant, funded by the Korea government (MSIT) (Grant No. NRF-2021M3H4A1A02049904).

## Conflict of Interest

The authors declare no conflict of interest.

## Data Availability Statement

The data that support the findings of this study are available from the corresponding author upon reasonable request.

## Keywords

2D materials, electrolyte insertion, H<sub>2</sub> bubble formation, hydrogen evolution reaction (HER), molybdenum sulfide (MoS<sub>2</sub>)

Received: July 4, 2022

Revised: September 2, 2022

Published online:

[1] I. Roger, M. A. Shipman, M. D. Symes, *Nat. Rev. Chem.* **2017**, *1*, 0003.

[2] V. R. Stamenkovic, D. Strmcnik, P. P. Lopes, N. M. Markovic, *Nat. Mater.* **2017**, *16*, 57.

- [3] J. D. Benck, T. R. Hellstern, J. Kibsgaard, P. Chakhranont, T. F. Jaramillo, *ACS Catal.* **2014**, *4*, 3957.
- [4] T. F. Jaramillo, K. P. Jørgensen, J. Bonde, J. H. Nielsen, S. Horch, I. Chorkendorff, *Science* **2007**, *317*, 100.
- [5] Q. Tang, D.-E. Jiang, *ACS Catal.* **2016**, *6*, 4953.
- [6] M. A. R. Anjum, H. Y. Jeong, M. H. Lee, H. S. Shin, J. S. Lee, *Adv. Mater.* **2018**, *30*, 1707105.
- [7] H. Li, C. Tsai, A. L. Koh, L. Cai, A. W. Contryman, A. H. Fragapane, J. Zhao, H. S. Han, H. C. Manoharan, F. Abild-Pedersen, J. K. Nørskov, X. Zheng, *Nat. Mater.* **2016**, *15*, 48.
- [8] M. Liu, M. S. Hybertsen, Q. Wu, *Angew. Chem., Int. Ed.* **2020**, *132*, 14945.
- [9] X. Wang, Y. Zhang, H. Si, Q. Zhang, J. Wu, L. Gao, X. Wei, Y. Sun, Q. Liao, Z. Zhang, K. Ammarah, L. Gu, Z. Kang, Y. Zhang, *J. Am. Chem. Soc.* **2020**, *142*, 4298.
- [10] J. Xie, H. Zhang, S. Li, R. Wang, X. Sun, M. Zhou, J. Zhou, X. W. Lou, Y. Xie, *Adv. Mater.* **2013**, *25*, 5807.
- [11] J. Hu, B. Huang, C. Zhang, Z. Wang, Y. An, D. Zhou, H. Lin, M. K. H. Leung, S. Yang, *Energy Environ. Sci.* **2017**, *10*, 593.
- [12] J. Kibsgaard, Z. Chen, B. N. Reinecke, T. F. Jaramillo, *Nat. Mater.* **2012**, *11*, 963.
- [13] J. Zhang, F. Dong, C. Wang, J. Wang, L. Jiang, C. Yu, *ACS Appl. Mater. Interfaces* **2021**, *13*, 32435.
- [14] S. K. Mazloomi, N. Sulaiman, *Renewable Sustainable Energy Rev.* **2012**, *16*, 4257.
- [15] G. Wosiak, J. da Silva, S. S. Sena, R. N. de Andrade, E. Pereira, *Chem. Eng. J.* **2022**, *433*, 133194.
- [16] A. Angulo, P. van der Linde, H. Gardeniers, M. Modestino, D. F. Rivas, *Joule* **2020**, *4*, 555.
- [17] G. R. Bhimanapati, T. Hankins, Y. Lei, R. A. Vilá, I. Fuller, M. Terrones, J. A. Robinson, *ACS Appl. Mater. Interfaces* **2016**, *8*, 22190.
- [18] G. Liu, W. S. Y. Wong, M. Kraft, J. W. Ager, D. Vollmer, R. Xu, *Chem. Soc. Rev.* **2021**, *50*, 10674.
- [19] Z. Ou, Z. Wang, B. Luo, E. Luijten, Q. Chen, *Nat. Mater.* **2020**, *19*, 450.
- [20] R. Serra-Maia, P. Kumar, A. C. Meng, A. C. Foucher, Y. Kang, K. Karki, D. Jariwala, E. A. Stach, *ACS Nano* **2021**, *15*, 10228.
- [21] Z.-W. Yin, S. B. Betzler, T. Sheng, Q. Zhang, X. Peng, J. Shangguan, K. C. Bustillo, J.-T. Li, S.-G. Sun, H. Zheng, *Nano Energy* **2019**, *62*, 507.
- [22] T.-H. Shen, L. Spillane, J. Peng, Y. Shao-Horn, V. Tileli, *Nat. Catal.* **2022**, *5*, 30.
- [23] J. Yang, M. K. Choi, Y. Sheng, J. Jung, K. Bustillo, T. Chen, S.-W. Lee, P. Ercius, J. H. Kim, J. H. Warner, E. M. Chan, H. Zheng, *Nano Lett.* **2019**, *19*, 1788.
- [24] Z. Ou, L. Yao, H. An, B. Shen, Q. Chen, *Nat. Commun.* **2020**, *11*, 4555.
- [25] G. Dunn, V. P. Adiga, T. Pham, C. Bryant, D. J. Horton-Bailey, J. N. Belling, B. LaFrance, J. A. Jackson, H. R. Barzegar, J. M. Yuk, S. Aloni, M. F. Crommie, A. Zettl, *ACS Nano* **2020**, *14*, 9637.
- [26] J. Kim, H. Seung, D. Kang, J. Kim, H. Bae, H. Park, S. Kang, C. Choi, B. K. Choi, J. S. Kim, T. Hyeon, H. Lee, D.-H. Kim, S. Shim, J. Park, *Nano Lett.* **2021**, *21*, 9153.
- [27] H. Li, Q. Zhang, C. C. R. Yap, B. K. Tay, T. H. T. Edwin, A. Olivier, D. Baillargeat, *Adv. Funct. Mater.* **2012**, *22*, 1385.
- [28] J. Zhang, J. Wu, H. Guo, W. Chen, J. Yuan, U. Martinez, G. Gupta, A. Mohite, P. M. Ajayan, J. Lou, *Adv. Mater.* **2017**, *29*, 1701955.
- [29] W. Wang, T. Xu, J. Chen, J. Shangguan, H. Dong, H. Ma, Q. Zhang, J. Yang, T. Bai, Z. Guo, H. Fang, H. Zheng, L. Sun, *Nat. Mater.* **2022**, *21*, 859.
- [30] P. Snapp, J. M. Kim, C. Cho, J. Leem, M. F. Haque, S. Nam, *NPG Asia Mater.* **2020**, *12*, 22.
- [31] W. Zhou, X. Zou, S. Najmaei, Z. Liu, Y. Shi, J. Kong, J. Lou, P. M. Ajayan, B. I. Yakobson, J.-C. Idrobo, *Nano Lett.* **2013**, *13*, 2615.
- [32] W. Zhou, L. Dong, L. Tan, Q. Tang, *Nanotechnology* **2021**, *32*, 145718.

- [33] X. Liu, X. Jiang, G. Shao, H. Xiang, Z. Li, Y. Jin, Y. Chen, H. Jiang, H. Li, J. Shui, Y. Feng, S. Liu, *Small* **2022**, *18*, 2200601.
- [34] Z. Lu, W. Zhu, X. Yu, H. Zhang, Y. Li, X. Sun, X. Wang, H. Wang, J. Wang, J. Luo, X. Lei, L. Jiang, *Adv. Mater.* **2014**, *26*, 2683.
- [35] B. Łosiewicz, R. Jurczakowski, A. Lasia, *Electrochim. Acta* **2012**, *80*, 292.
- [36] A. Krull, T.-O. Buchholz, F. Jug, in *2019 IEEE/CVF Conf. Computer Vision and Pattern Recognition (CVPR)*, IEEE, Piscataway, NJ, USA **2019**, p. 2124–2132.
- [37] A. Paszke, S. Gross, F. Massa, A. Lerer, J. Bradbury, G. Chanan, T. Killeen, Z. Lin, N. Gimelshein, L. Antiga, A. Desmaison, A. Kopf, E. Yang, Z. DeVito, M. Raison, A. Tejani, S. Chilamkurthy, B. Steiner, L. Fang, J. Bai, S. Chintala, in *Advances in Neural Information Processing Systems 32 (NeurIPS 2019)* (Eds: H. Wallach, H. Larochelle, A. Beygelzimer, F. d'Alché-Buc, E. Fox, R. Garnett), NeurIPS, La Jolla, CA, USA **2019**, p. 8024.
- [38] W. Falcon, *GitHub*, <https://github.com/PyTorchLightning/pytorch-lightning> (accessed: December 2021).
- [39] B. Hess, C. Kutzner, D. van der Spoel, E. Lindahl, *J. Chem. Theory Comput.* **2008**, *4*, 435.
- [40] S. Pronk, S. Páll, R. Schulz, P. Larsson, P. Bjelkmar, R. Apostolov, M. R. Shirts, J. C. Smith, P. M. Kasson, D. van der Spoel, B. Hess, E. Lindahl, *Bioinformatics* **2013**, *29*, 845.
- [41] L. S. Dodda, I. Cabeza de Vaca, J. Tirado-Rives, W. L. Jorgensen, *Nucleic Acids Res.* **2017**, *45*, W331.
- [42] L. S. Dodda, J. Z. Vilseck, J. Tirado-Rives, W. L. Jorgensen, *J. Phys. Chem. B* **2017**, *121*, 3864.
- [43] W. L. Jorgensen, J. Tirado-Rives, *Proc. Natl. Acad. Sci. USA* **2005**, *102*, 6665.
- [44] V. Sresht, A. G. Rajan, E. Bordes, M. S. Strano, A. A. H. Pádua, D. Blankschtein, *J. Phys. Chem. C* **2017**, *121*, 9022.
- [45] I. G. Tironi, R. M. Brunne, W. F. van Gunsteren, *Chem. Phys. Lett.* **1996**, *250*, 19.
- [46] S. Mitra, A. Kabiraj, S. Mahapatra, *npj 2D Mater. Appl.* **2021**, *5*, 33.
- [47] T. Darden, D. York, L. Pedersen, *J. Chem. Phys.* **1993**, *98*, 10089.
- [48] B. Hess, H. Bekker, H. J. C. Berendsen, J. G. E. M. Fraaije, *J. Comput. Chem.* **1997**, *18*, 1463.
- [49] S. Nosé, *Mol. Phys.* **1984**, *52*, 255.
- [50] W. G. Hoover, *Phys. Rev. A* **1985**, *31*, 1695.
- [51] M. Parrinello, A. Rahman, *J. Appl. Phys.* **1981**, *52*, 7182.